Atmos. Chem. Phys., 18, 17475–17488, 2018
https://doi.org/10.5194/acp-18-17475-2018

Atmospheric Chemistry and Physics
Open Access
EGU

The efficacy of aerosol–cloud radiative perturbations from near-surface emissions in deep open-cell stratocumuli

Anna Possner[1], **Hailong Wang**[2], **Robert Wood**[3], **Ken Caldeira**[1], **and Thomas P. Ackerman**[3,4]

[1]Department of Global Ecology, Carnegie Institution for Science, Stanford, USA
[2]Earth Systems Analysis & Modeling, Pacific Northwest National Laboratory, Richland, USA
[3]Department of Atmospheric Scieces, University of Washington, Seattle, USA
[4]Joint Institute for the Study of Atmosphere and Ocean, University of Washington, Seattle, USA

Correspondence: Anna Possner (apossner@carnegiescience.edu)

Received: 11 July 2018 – Discussion started: 30 July 2018
Revised: 10 October 2018 – Accepted: 19 November 2018 – Published: 11 December 2018

Abstract. Aerosol–cloud radiative effects are determined and quantified in simulations of deep open-cell stratocumuli observed during the VAMOS Ocean-Cloud-Atmosphere-Land Study Regional Experiment (VOCALS-REx) campaign off the west coast of Chile. The cloud deck forms in a boundary layer 1.5 km deep, with cell sizes reaching 50 km in diameter. Global databases of ship tracks suggest that these linear structures are seldom found in boundary layers this deep. Here, we quantify the changes in cloud radiative properties to a continuous aerosol point source moving along a fixed emission line releasing 10^{17} particles per second. We show that a spatially coherent cloud perturbation is not evident along the emission line. Yet our model simulates an increase in domain-mean all-sky albedo of 0.05, corresponding to a diurnally averaged cloud radiative effect of $20\,\mathrm{W\,m^{-2}}$, given the annual mean solar insolation at the VOCALS-REx site. Therefore, marked changes in cloud radiative properties in precipitating deep open cells may be driven by anthropogenic near-surface aerosol perturbations, such as those generated by ships.

Furthermore, we demonstrate that these changes in cloud radiative properties are masked by the naturally occurring variability within the organised cloud field. A clear detection and attribution of cloud radiative effects to a perturbation in aerosol concentrations becomes possible when sub-filtering of the cloud field is applied, using the spatio-temporal distribution of the aerosol perturbation. Therefore, this work has implications for the detection and attribution of effective cloud radiative forcing in marine stratocumuli, which constitutes one of the major physical uncertainties within the climate system. Our results suggest that ships may sometimes have a substantial radiative effect on marine clouds and albedo, even when ship tracks are not readily visible.

1 Introduction

Aerosol–cloud interactions (aci) in low-level clouds, which span just over a fifth of the Earth's ocean surface (Wood, 2012), contribute the largest uncertainty to estimates of global mean effective radiative forcing (ERF) of anthropogenic aerosols (Myhre et al., 2013). Current estimates of $\mathrm{ERF_{aci}}$ range from $-1.2\,\mathrm{W\,m^{-2}}$, which would constitute a strong global cooling that would partially offset the effects of warming due to anthropogenic greenhouse gas emissions, to $0.0\,\mathrm{W\,m^{-2}}$, which would render these effects negligible at the global scale (Boucher et al., 2013).

To reduce this uncertainty substantially through the use of satellite retrievals and global climate models (GCMs) remains challenging. These challenges include issues of collocation in retrievals of aerosol and cloud properties from space (Koren et al., 2007; Charlson et al., 2007), and the inadequate representation of small-scale dynamical processes that contribute to the cloud response in coarse-scale models (Nam et al., 2012; Schneider et al., 2017). Valuable insights into the processes involved and plausible ranges of cloud radiative perturbations through aerosols have been obtained by the study of ship tracks. These *anomalous cloud lines* (Conover, 1966) are a phenomenon associated with a characteristic spatial structure, which occurs in low-level

stratocumulus clouds. The changed cloud radiative properties within these tracks can be attributed to localised aerosol perturbations (Durkee et al., 2000a, c; Schreier et al., 2006).

Databases obtained from satellite retrievals (Coakley and Walsh, 2002; Christensen and Stephens, 2012; Chen et al., 2015), as well as high-resolution modelling studies (Wang and Feingold, 2009; Wang et al., 2011; Berner et al., 2015), show that the net cloud radiative effect (CRE) in individual ship tracks does not depend only on cloud droplet number increases and size decreases, which occur in almost all cases (Chen et al., 2012), but also on induced changes in cloud morphology, cloud fraction (CF) and liquid water path (LWP). Cloud albedo (A_{cld}) may not always increase with increased levels of pollution, but may also decrease (Christensen and Stephens, 2012; Berner et al., 2015). Furthermore, localised gradients in aerosol concentration have been shown to induce self-sustaining mesoscale circulations (Chen et al., 2015; Wang et al., 2011), by the local suppression of precipitation in the polluted cloud and the convergence of cold pools transporting moisture into the polluted cloud from the surrounding precipitating clouds. In the global mean, LWP increases of between 16 % and 24 % (depending on above-cloud moisture content) were found in ship tracks that formed within the precipitating cloud regime (Toll et al., 2017).

However, ship tracks are rare in comparison to the number of ocean-going ships that criss-cross the world's oceans (Schreier et al., 2007). Merely 1924 ship tracks were detected over 2 years worldwide (Campmany et al., 2009), while the total ocean-going fleet consists of over 50 000 ships that exceed 500 gross tons in weight (European Maritime Safety Agency, 2014). Understanding what constrains their occurrence in terms of background pollution, boundary layer dynamics and large-scale stability may facilitate constraining regimes and magnitudes of global effective radiative forcing estimates. In particular, studies of ship tracks in high-resolution models and satellite retrievals have been mostly limited to extremely shallow boundary layers that range in depth from 300 to 600 m (Christensen and Stephens, 2012; Berner et al., 2015; Chen et al., 2015). Ship track formation within one slightly deeper boundary layer of 800 m was investigated in high-resolution simulations by Wang and Feingold (2009) and Wang et al. (2011). Indeed ship tracks are very rarely detected in satellite retrievals of boundary layers deeper than 800 m (Durkee et al., 2000b; Toll et al., 2017). Yet over 70 % of stratocumulus clouds are found in deeper boundary layers (Muhlbauer et al., 2014).

The potential for albedo changes is particularly high in the open-cell and disorganised stratocumulus regimes, which occur more frequently in the subtropics, than in the closed-cell regime (Muhlbauer et al., 2014). Both of these regimes are characterised by shallow convective cloud structures that detrain laterally at the cloud top. The detrained cloud sheets that span the regions between the convective structures are optically thin (cloud optical thickness $\tau < 3$), are often associated with low droplet number concentrations ($N_{\mathrm{d}} \sim 5\,\mathrm{cm}^{-3}$) and may contribute substantially to the overall cloud fraction (Wood et al., 2018). Thus, their albedo is highly susceptible to aerosol perturbations from the perspective of Platnick and Twomey's (1994) albedo susceptibility definition. Yet, the efficacy of aerosol–cloud radiative interactions within these detrained cloud segments remains unclear. In general, the processes governing aerosol–cloud interactions in deep stratocumulus boundary layers remain weakly constrained, with only few process-level studies (Wang et al., 2010; Kazil et al., 2011; Wood et al., 2011b; Zuidema et al., 2016) that quantify effects on cloud characteristics through aerosol pollution.

Within this study we quantify changes in cloud radiative properties due to aerosol perturbations in deep (boundary layer depth of ~ 1.5 km) open-cell stratocumulus clouds and discuss dominant mechanisms that constrain the cloud albedo response.

2 Methodology

2.1 Case description

This study is based on a well-documented case of open-cell stratocumulus clouds embedded within a boundary layer ~ 1.5 km deep, which was observed during research flight 6 of the VAMOS Ocean-Cloud-Atmosphere-Land Study Regional Experiment (VOCALS-REx) campaign. Detailed information on the particular case and measurement techniques can be found in Wood et al. (2011a) and Wood et al. (2011b) respectively. Here we give an overview of the two cloud regimes and their characteristics relevant to this study.

The cloud regime was sampled during the early morning hours (03:00 to 08:30 local time) on 28 October 2008. A summary of cloud properties measured during the campaign is given in Table 1. The characteristic cell size was found to be between 30 and 40 km, which is detected frequently in southeast Pacific stratocumulus clouds (Wood and Hartmann, 2006). A cloud fraction of 56 % was measured in the open-cell regime, which is consistent with the observed high level of detrained cloudy air masses, which spread from the updraft cores into the inner regions of the cell. Furthermore, a cloud cover of this extent is typical for marine open-cell stratocumuli (Muhlbauer et al., 2014; Terai et al., 2014).

The open-cell clouds coincided with moister sub-cloud layer air masses, as compared to the neighbouring closed-cell regime, and were characterised by low sub-cloud layer aerosol concentrations ($30\,\mathrm{cm}^{-3}$). A strong vertical gradient in aerosol concentration was observed within the open cells near the cloud base where concentrations decreased rapidly. A strong horizontal gradient in cloud-top droplet number concentration ($N_{\mathrm{d\_top}}$) was observed (Wood et al., 2011a) between the updraft cores ($N_{\mathrm{d\_top}} \sim 30\,\mathrm{cm}^{-3}$) and the detrained cloud filaments ($N_{\mathrm{d\_top}} \sim 1$–$10\,\mathrm{cm}^{-3}$). Substantial rates of

Table 1. Spatio-temporal averages of liquid water path (LWP), surface precipitation (R_{sfc}), cloud base precipitation (R_{cb}), cloud fraction (CF), sub-cloud mean boundary layer aerosol concentration (N_{a_sub}) and cloud-top droplet number concentration (N_{d_top}) are presented. The first row containing data shows the observations of the open-cell stratocumulus deck obtained during research flight RF06 of the VOCALS-Rex campaign on 28 October 2008 between 08:00 and 13:30 UTC. The numerical results, shown in the last two rows, were averaged over the identical time periods over both simulated days. Domain-mean values were computed for LWP, CF and N_{a_sub}. R_{sfc} was averaged only over values exceeding 0.1 mm day^{-1} and R_{cb} was averaged for all $R_{cb} > 0$ mm day^{-1} (consistent with observations). N_{d_top} was diagnosed at the highest model level where cloud water content exceeded 0.01 g m^{-3} and was averaged horizontally (cloudy points only). Numbers in brackets denote the interquartile range of each variable, which covers the spatial and temporal variability of the cloud field. Numerical results are shown for the control simulation (ctrl) and the aerosol perturbed simulation (ship). Further details on simulations can be obtained in the text.

08:00–13:30 UTC averages						
Sim/obs	LWP (g m^{-2})	R_{sfc} (mm day^{-1})	R_{cb} (mm day^{-1})	CF (%)	N_{a_sub} (cm^{-3})	N_{d_top} (cm^{-3})
RF06	141	1	4–5	56	30	10
ctrl	75 [6, 70]	4.2 [0.2, 2.4]	9.1 [0.1, 2.9]	50	34 [32, 37]	8 [3, 11]
ship	82 [10, 81]	4.1 [0.2, 2.2]	8.6 [0.1, 2.9]	57	45 [32, 42]	12 [3, 13]

drizzle were observed at cloud base. Yet over 50 % evaporated before reaching the surface.

2.2 Simulation set-up

Two simulations were performed using the Weather Research and Forecasting (WRF) model at the convection-resolving scale, with a horizontal grid resolution of 300×300 m^2, a vertical resolution of 30 m and a time step of 3 s following Wang et al. (2010). The idealised simulations with periodic boundary conditions at the domain edges were initialised with meteorological profiles obtained during research flight 6 of the VOCALS-REx field campaign (Wang et al., 2011; Wood et al., 2011a). A brief overview of the research flight is given in Sect. 2.1. Given the large characteristic spatial scales of the cellular organisation of the cloud field, with cell sizes ranging from 30 to 40 km, simulations were performed on a large domain of 180×180 km^2. The domain was centred on 78° W and 15° S, which is off the west coast of Chile. The model top was specified at an altitude of 2 km, which is 600 m above the boundary layer top. Above this height a standard clear-sky atmosphere profile is assumed for the computation of the radiative fluxes until the top of atmosphere.

Both simulations were run for 48 h with a fixed divergence rate of 1.67×10^{-6} s^{-1}, which was estimated from QuickSCAT surface winds (NASA, 2012) and prescribed surface fluxes. Surface latent heat and sensible heat fluxes were specified, according to field measurements, as 120 and 15 W m^{-2} (defined as positive upward) respectively. The surface pressure was specified as 1018 hPa. For simplicity, mean advective tendencies in the wind field were removed from the soundings.

The simulations were performed with the two-moment (Morrison et al., 2009) microphysics scheme, with a prognostic treatment of number and mass concentrations for cloud water and rain. The exponents of the cloud liquid water content and N_d in the Khairoutdinov and Kogan (2000) autoconversion rate were adjusted to values obtained from the VOCALS-REx field campaign as 3.19 (cloud water exponent) and -1.49 (N_d exponent) respectively. These exponents were obtained for the VOCALS-REx field data using the approach described in Wood (2005). Precipitation formation was artificially suppressed in the first 2 h of simulation to facilitate a thermodynamic adjustment to the initialisation sounding before including moisture sinks. Cloud condensation nuclei (CCN) were treated as in Wang et al. (2011) with a prognostic log-normal sea salt mode centred at a mean diameter of 500 nm and variance of 1.5. Aerosols were advected according to grid-scale and subgrid-scale transport tendencies, and aerosol–cloud interactions were included by removing aerosols upon activation, which was treated as in Kravitz et al. (2014). The release of aerosol upon complete evaporation of cloud droplets and rain drops was also simulated. A surface sea salt emission flux of 20 m^{-2} h^{-1} was specified in line with estimates from previous simulations (Wang et al., 2010; Kazil et al., 2011).

In addition to the control simulation, from here on named *ctrl* simulation, an aerosol perturbation experiment was designed. The simulation, named *ship* simulation, followed the set-up of Wang et al. (2011) for direct comparison between the deep boundary layer case and shallow boundary layer case in terms of aerosol–cloud radiative perturbations. A ship moving at 5 m s^{-1} through the centre of the domain was allowed to continuously emit sea salt at a rate of 10^{17} s^{-1} and a mean dry radius of 300 nm. This flux was chosen to match emissions within a previously studied case within a shallow open-cell regime (Wang et al., 2011) (see Sect. 3.2.1 for an in-depth discussion). Furthermore, these emissions were consistent with estimates proposed by Salter et al. (2008) for marine cloud brightening applications. The Community Atmosphere Model (CAM) radiation scheme was used in the simulations and A_{cld} was estimated as $A_{cld} = \tau/(\tau + 6.8)$, where τ denotes the cloud optical depth, which in turn was

diagnosed as

$$\tau = \int_{z=0}^{\infty} \frac{3q_l}{2\rho_w R_{eff}} dz, \quad (1)$$

where ρ_w is 997.0 kg m^{-3}, q_l is liquid water content, R_{eff} is effective cloud droplet radius and z is height. The cloud base precipitation rate (R_{cb}) was computed as the mean precipitation flux across the lowest third of the cloud vertical extent, which is consistent with its estimation from observations.

3 Results

3.1 Evaluation of open-cell characteristics

In order to assess the radiative effect of concentrated and localised aerosol pollution on deep open-cell clouds, the simulations need to demonstrate sufficient skill in capturing the characteristics and dynamics of the open-cell regime. Following initialisation, an unorganised stratiform cloud deck formed in the ctrl simulation. Initial organised structures appeared 6 h after initialisation following the onset of precipitation (Fig. 1). Following the second night, observed length scales of organisation (see Sect. 2.1) were simulated.

The diurnal evolution of LWP and N_{d_top} is shown in Fig. 1. Periods when R_{cb} exceeds 3 mm day^{-1} are marked in white. The simulation showed a pronounced diurnal cycle during both days in LWP and R_{cb}. As in Wang et al. (2010), solar heating was found to break up the cell walls, which led to a reduction of LWP in the upper percentiles, a reduction in cloud-base precipitation rates to $R_{cb} < 2$ mm day^{-1} and consequently the loss of cloud-field organisation in the late afternoon. During the night the cloud deck recovered and organisation was re-established.

The ctrl simulation was characterised by a well-mixed cloud layer and stably stratified sub-cloud layer (see Fig. S1 in the Supplement), which is characteristic of deep boundary layers. This structure developed rapidly following initialisation from the well-mixed state. Within the first 3.5 h the boundary layer deepened by 180 m before stabilising at 1.5 km, and the sub-cloud layer became stratified. A mean R_{cb} of 9.1 mm day^{-1} (Table 1) was simulated in the early morning hours of the VOCALS-REx field campaign.

Although simulated mean R_{cb} was within the spread of observed precipitation rates (Fig. S2), it was roughly twice as high as the mean R_{cb} rates inferred from observations (Table 1). Meanwhile, the mean LWP was underestimated by a factor of 2 in the open-cell regime, which is consistent with an overestimation in precipitation. However, the simulated cumulative precipitation distribution shown in the Supplement (Fig. S2a) showed that the overall distribution of R_{cb} was well captured in the ctrl simulation and that the bias in the mean originates from the slight overestimation of intense precipitation events exceeding 20 mm day^{-1}. These events are likely to be found within the walls of the open cells, which are characterised by strong updrafts (Fig. S2b).

The microphysical quantities, such as the mean sub-cloud layer aerosol concentration ($N_{a\_sub} = 34$ cm^{-3}) and $N_{d\_top} = 8$ cm^{-3}, were in good agreement with the observations. In the simulations the aerosol particles are lifted into the cloud layer within the cell walls, where they activated and N_d was relatively high. Cloud filaments, many of which are quite optically thin, were detrained horizontally, and are characterised by low N_{d_top} (Fig. 2a) due to the efficient removal through precipitation. While cell-wall N_d may reach up to 40 cm^{-3} in the ctrl simulation (Fig. 2b), characteristic N_d in detrained cloud filaments, sometimes referred to as "veil clouds" (Wood et al., 2018), were as low as 2–3 cm^{-3}. The efficient removal of aerosol particles through cloud processing combined with the stable stratification in the sub-cloud layer induced strong vertical gradients in the combined particle number concentration N_{tot} defined as $N_{tot} = N_a + N_d$, where N_a denotes the aerosol number concentration. Sub-cloud layer N_{tot} ranged between 30 and 60 cm^{-3}, while values below 10 cm^{-3} above the cloud base height were simulated frequently (Fig. 2c).

In summary, despite remaining biases in the mean LWP and R_{cb}, the simulation overall captured a realistic evolution of the open-cell cloud deck with a pronounced diurnal cycle. Since the overall cloud-cell statistics (Table 1) and the horizontal cloud cover are consistent with observations, it gives us confidence that the underlying cloud dynamics were captured in the ctrl simulation. Regions of detrained cloud spanned 36 % of the domain, and were characterised by low in-cloud LWP and N_{d_top}, which makes them particularly susceptible to aerosol-induced cloud radiative perturbations. Yet any near-surface source of pollution will predominantly be transported into the cloud layer through the cell walls given the pronounced vertical stratification in the sub-cloud layer, where wet aerosol removal processes are efficient. It therefore remains to be seen whether substantial changes in cloud radiative properties can be induced by near-surface aerosol perturbations.

3.2 Efficacy of aerosol perturbation

The sea salt perturbed simulation displayed a spatially constrained aerosol plume meandering around the emission line (Fig. 3a). The highest values of N_{a_sub} exceeding 1000 cm^{-3} were found within a narrow plume extending in length up to 60 km behind the point source. Overall, the aerosol perturbation remained spatially constrained within the boundary layer in a region of ±30 km around the emission line. This strip of the domain (spanning 60–120 km in the y direction) is characterised by increased levels of N_{a_sub} and from here on will be referred to as "seeded", whereas the domain outside this region will be referred to as "unseeded".

Inside the seeded region the emitted aerosol was predominantly transported into the cloud within the updrafts of the

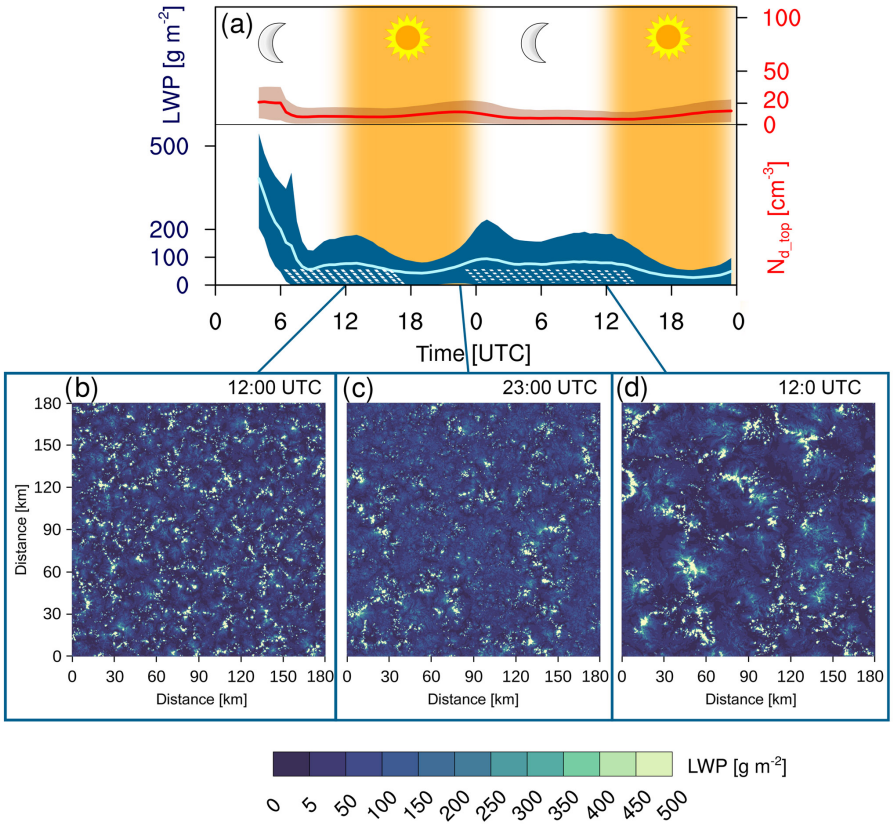

Figure 1. **(a)** Time series of domain-mean liquid water path, LWP (green), and cloud-top droplet number concentration, N_{d_top} (red), for the ctrl simulation. Shading (blue for LWP, black for N_{d_top}) denotes interdecile percentile range. Snapshots of LWP are shown in **(b)** after initial organised structures developed, **(c)** after the solar maximum and **(d)** for the second day organised state.

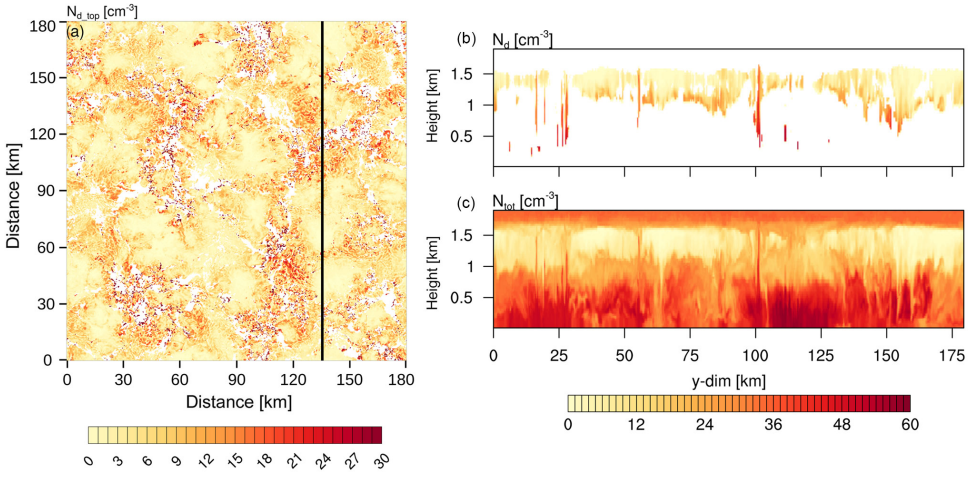

Figure 2. **(a)** Instantaneous cloud-top droplet number concentration, N_{d_top} (corresponding snapshot to LWP field shown in Fig. 1d). The black line denotes the location of the cross section of **(b)** cloud droplet number concentration (N_d) and **(c)** total number concentration ($N_{tot} = N_a + N_d$, where N_a denotes the aerosol number concentration). Cloud top is defined as in Table 1.

cell walls (Fig. S3). Despite efficient wet removal processes within the cell walls, the largest absolute changes in N_d were as large as 600 cm^{-3}. At the cloud top, increases in N_{d_top} of up to 150 cm^{-3} were found (Fig. 3b). From the cell walls,

Table 2. Same as Table 1 but for mean values of the last 24 h period. The following additional variables were added to the table: cloud albedo (A_{cld}), all-sky albedo $A_{all} = CF \cdot A_{cld} + (1 - CF) \cdot A_{clr}$ and cloud-top effective cloud droplet radius (R_{eff_top}). A_{clr} denotes the clear-sky albedo, which was determined as $A_{clr} = 0.06$ in both simulations. R_{eff_top} was diagnosed similarly to N_{d_top} and averaged over cloudy regions only. For A_{all} and A_{cld} domain averages (i.e. including clear-sky and cloudy sky) are given. All entries for "wall" (cloud with updraft $> 0.5\,m\,s^{-1}$) and detrained (non-wall cloud) regions, denote in-cloud averages only. CF for wall and detrained cloud denotes the domain area fraction covered by each category. Inside cell walls and cloud filaments CF is 100 %. The seeded region is defined as ±30 km around the emission line and the remainder of the domain is classified as unseeded.

	Second day mean								
Sim/obs	LWP ($g\,m^{-2}$)	R_{sfc} ($mm\,day^{-1}$)	R_{cb} ($mm\,day^{-1}$)	A_{cld}	A_{all}	CF (%)	N_{a_sub} (cm^{-3})	N_{d_top} (cm^{-3})	R_{eff_top}
ctrl	64 [2, 57]	4.6 [0.2, 2.4]	8.4 [0.1, 2.3]	0.18 [< 0.01, 0.30]	0.22	44	36 [32, 39]	9 [3, 12]	21 [17, 26]
detrained	92 [38, 101]	4.5 [0.2, 2.6]	9.2 [0.3, 4.6]	0.37 [0.28, 0.43]	0.13	36	–	8 [3, 12]	23 [19, 27]
wall	331 [71, 449]	10.0 [0.4, 7.8]	33.7 [0.4, 18.5]	0.61 [0.45, 0.77]	0.05	8	–	13 [4, 18]	21 [17, 25]
ship	75 [10, 73]	4.5 [0.2, 2.1]	7.7 [0.1, 2.2]	0.26 [0.07, 0.41]	0.27	58	50 [33, 50]	14 [4, 17]	21 [16, 26]
seeded	87 [18, 88]	4.8 [0.2, 2.2]	7.6 [0.1, 2.0]	0.33 [0.16, 0.48]	0.35	72	77 [47, 81]	24 [6, 31]	18 [14, 22]
detrained	87 [38, 99]	4.1 [0.2, 2.1]	5.9 [0.1, 2.4]	0.43 [0.32, 0.52]	0.25	59	–	25 [7, 32]	19 [14, 22]
wall	254 [54, 307]	9.6 [0.3, 6.8]	24.6 [0.2, 8.1]	0.59 [0.43, 0.75]	0.08	13	–	36 [10, 46]	18 [14, 21]
unseeded	67 [5, 67]	4.3 [0.2, 2.1]	7.7 [0.1, 2.3]	0.21 [0.04, 0.36]	0.24	51	35 [31, 38]	9 [3, 11]	22 [18, 27]
detrained	92 [41, 104]	4.1 [0.2, 2.2]	8.1 [0.4, 4.1]	0.37 [0.29, 0.44]	0.16	43	–	8 [3, 11]	24 [19, 28]
wall	299 [68, 414]	9.6 [0.3, 7.1]	30.2 [0.4, 15.2]	0.57 [0.41, 0.73]	0.05	8	–	12 [4, 17]	22 [18, 26]

the increased levels of N_d persisted to the detrained cloud regions (Fig. S3), where the largest relative increases in N_{d_top} were found. On average N_{d_top} increased by 177 % within the cell walls and by 213 % within the stratified detrained cloud (Table 2). In this analysis cell walls were diagnosed as cloud-covered regions with updraft speeds exceeding $0.5\,m\,s^{-1}$. All remaining, non-wall cloudy grid points were classified as detrained cloud.

The largest decreases in the cloud droplet effective radius at the cloud top (R_{eff_top}) were found to coincide with regions of large increases in N_{d_top} (Fig. 3c and b respectively). R_{eff_top} may be reduced by up to 10 µm locally. The largest decreases in R_{eff_top} were found within the vicinity of strong updrafts. Here, many aerosols were carried into the cloud layer and were activated. Efficient in-cloud scavenging led to a reduction in N_{d_top} and an increase in R_{eff_top} going radially outward from the centre of the updraft cores. Averaged over the seeded domain, a mean reduction in R_{eff_top} between 3 and 4 µm was simulated in the cell walls and detrained cloud regions (Table 2).

The changes in cloud-microphysical properties led to an increase in domain-averaged LWP (Table 2) within the seeded (36 %) and unseeded regions (5 %). Yet lower mean-values of in-cloud LWP were found within the detrained cloud and cell-wall regimes in both domains of the ship simulation (Table 2). R_{cb} was found to decrease by $0.7\,mm\,day^{-1}$, while R_{sfc} remained largely unaffected by the aerosol perturbation (Table 2).

Due to the reduction in R_{cb}, more cloud water was retained within the updraft and detrained horizontally into the stratified cloud filaments, which penetrated deeper into the open cells. The increase in areal extent of the detrained cloud sheets was accompanied by a shift (Fig. S5) in in-cloud LWP distribution towards lower LWP between 50 and $150\,g\,m^{-2}$. Therefore, the increase in domain-mean LWP, despite the decrease in in-cloud LWP, was attributed to the 14 % increase in cloud fraction from 44 % in the ctrl simulation to 58 % in the ship simulation (Table 2). Yet the open cells remain partially uncovered, which prevents a potential transition from the open-cell state to the closed-cell regime.

Mean A_{cld} is increased by 0.15 from 0.18 in the ctrl simulation to 0.33 inside the seeded region of the ship simulation (Table 2). This translates to a change in all-sky albedo (A_{all}) of 0.11 inside the seeded region, which corresponds to a shortwave cloud radiative effect (SW CRE) of $44\,W\,m^{-2}$ at an annual mean solar insolation of $404\,W\,m^{-2}$ at the VOCALS-REx field site. Although the strongest increase in A_{all} was confined to the seeded domain, A_{all} was found to be increased throughout the simulation domain (Fig. S6). Averaged over the entire domain A_{all} increased by 0.05, which is equivalent to a SW CRE of $20\,W\,m^{-2}$ exerted over an area of $180 \times 180\,km^2$.

The changes in domain-mean A_{all} were attributed to albedo changes of the detrained cloud sheets spanning the domain between the cell walls. Both the areal coverage and reflectivity of the detrained cloud sheets increased in the ship simulation as compared to the ctrl simulation (Table 2). Meanwhile, the cell-wall albedo of 0.6 remained unaffected by the aerosol perturbation. Furthermore, we attributed the simulated change in A_{all} predominantly to adjustments in macrophysical cloud properties of the detrained cloud regions. Changes in cloud microphysical properties and the associated Twomey (1991) effect were found to be of secondary importance to the change in all-sky albedo.

The increase in cloud fraction alone, while assuming no further changes in in-cloud A_{cld} (i.e. assuming A_{cld} as in the ctrl detrained and cell-wall regions in Table 2 and multiplying these values by the areal coverage of wall and de-

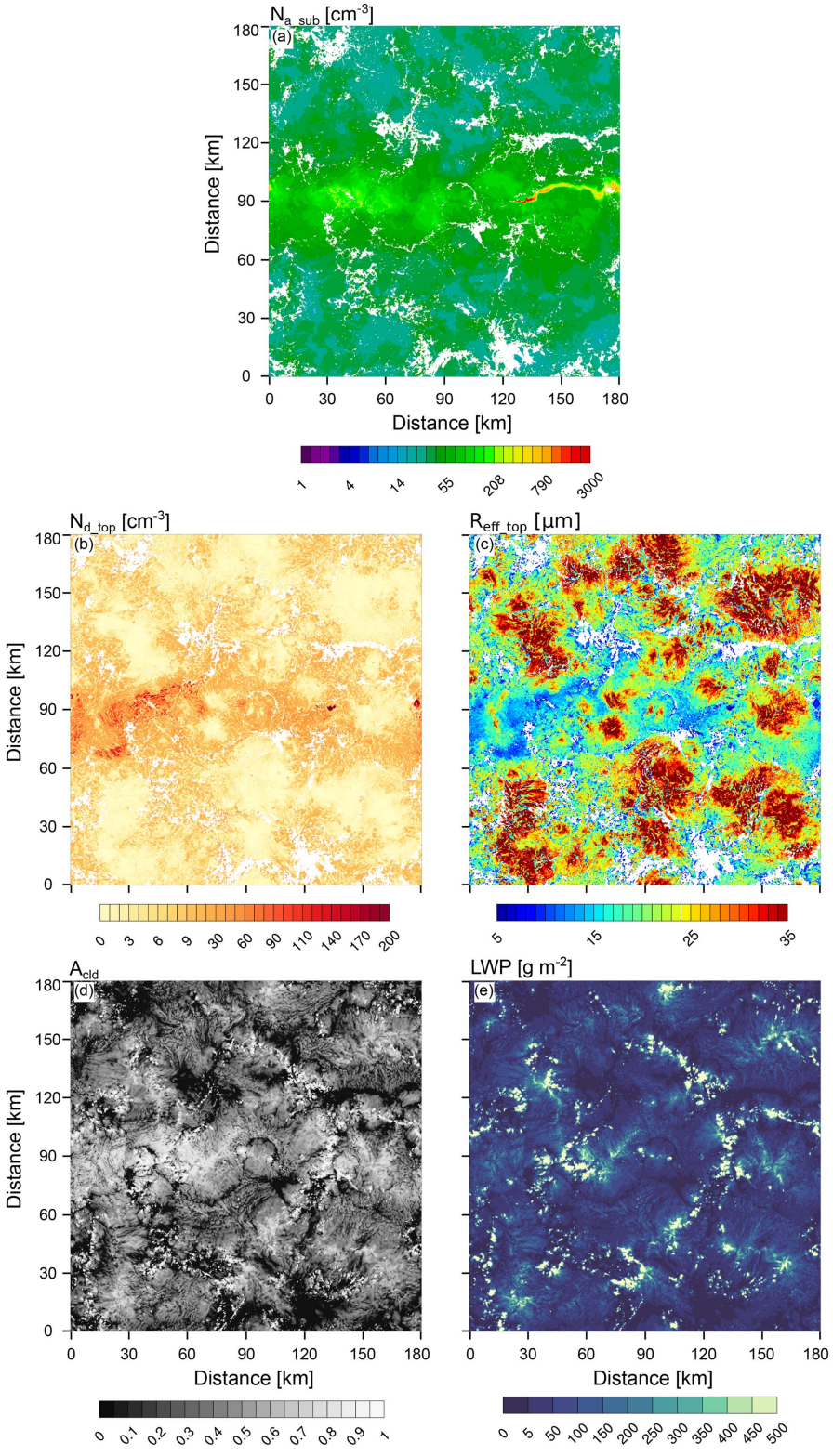

Figure 3. Snapshots of **(a)** vertically averaged sub-cloud layer aerosol concentration (N_{a_sub}), **(b)** cloud-top cloud droplet number concentration (N_{d_top}), **(c)** cloud-top mean effective cloud droplet radius (R_{eff_top}), **(d)** cloud albedo (A_{cld}) and **(e)** liquid water path (LWP). Instantaneous fields are shown at 12:00 UTC for the ship simulation. Fields for the ctrl simulation are shown in the Supplement (Fig. S4).

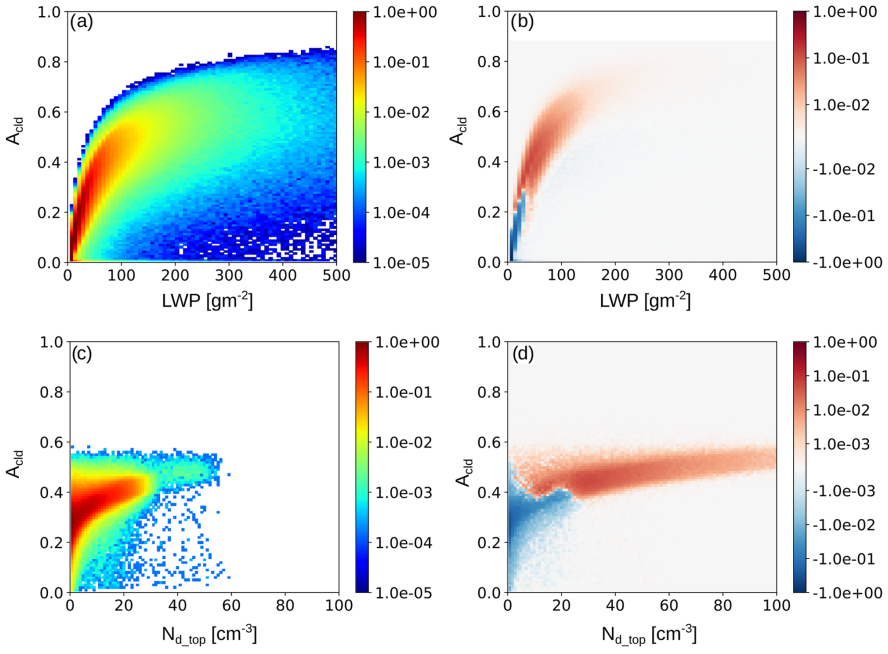

Figure 4. Occurrence rate F (%) for the **(a)** liquid water path (LWP) versus cloud albedo (A_{cld}) phase space and **(c)** the cloud-top droplet number concentration (N_{d_top}) versus A_{cld} phase space. The N_{d_top}–A_{cld} space was sub-filtered for LWP within the range of 40–60 g m^{-2}. Results are shown in **(a)** and **(c)** for the last 24 h of the ctrl simulation. Absolute changes in F for the ship simulation with respect to the ctrl simulation are shown in **(b)** and **(d)** respectively. F is normalised to 100 % across the shown phase space. The bin widths for each of which F is defined are ΔLWP: 7 g m^{-2}, ΔN_{d_top}: 1 cm^{-3} and ΔA_{cld}: 0.01.

trained cloud regions of the ship simulation), accounted for 90 % (100 %) of the increase in domain-averaged A_{cld} inside the seeded (unseeded) domain. The additional increase in domain-mean A_{cld} within the seeded domain was attributed to the increase in A_{cld} from 0.37 to 0.43 within the cloud filaments of the ship simulation (Table 2).

Figure 4 shows the normalised occurrence rate (F) within the detrained cloud regions. F, and the change in F due to the aerosol perturbation, is shown for each bin within the LWP–A_{cld} phase space (Fig. 4a and b respectively). The behaviour of F within the N_{d_top}–A_{cld} space, which was sub-filtered to only include points where in-cloud LWP ranged between 40 and 60 g m^{-2}, is shown in Fig. 4c and d. The behaviour of F for other LWP sub-ranges was found to be qualitatively similar (Fig. S7).

The increased occurrence of moderate LWP values (50 $\leq$ LWP $<$ 150 g m^{-2}) may locally coincide with an increase in A_{cld} (Fig. 4b). Yet the overall decrease in in-cloud LWP by 5 %–23 % (Table 2) implied that the increase in A_{cld} within the cloud filaments could not be attributed to LWP adjustments. If anything, A_{cld} would be expected to decrease given the reduction in in-cloud LWP. Meanwhile, Fig. 4d displays a clear shift in F towards higher N_{d_top} associated with locally increased A_{cld}. Hence, the increase in in-cloud A_{cld} was attributed to the Twomey (1991) effect within the stratified cloud.

3.2.1 Contrasting the cloud response in deep and shallow open cells

Although the areal coverage of the detrained cloud amount between the cell walls of the open cells increased, which contributed to the brightening of the cloud deck, the highly concentrated aerosol perturbation was insufficient to induce a transition from open to closed cells in these simulations. Aerosols may impact this transition via aerosol–precipitation interactions. Decreases in N_a from 90 to 10 cm^{-3} facilitated a rapid transition from the closed-cell to the open-cell state (Feingold et al., 2015) in previous simulations within the 800 m deep boundary layer observed during DYCOMS-II. Yet, the reverse transition from the open-cell state to the closed-cell state occurred over far longer timescales, if at all (Wang and Feingold, 2009; Feingold et al., 2015). Nonetheless, strongly concentrated sea salt emissions of 10^{17} particles s^{-1} within the same boundary layer induced a transition from the open-cell to a filled-in cloud-cell state along the seeding line. Along the seeding line a secondary circulation maintained the cloud layer within the track while depleting the surrounding cloud (Wang et al., 2011). Such transitions from open cells to a closed-cell state along ship tracks have also been observed using remote sensing (Goren and Rosenfeld, 2012).

While a ship track formed in the shallow boundary layer with open cells between 10 and 15 km in size (Fig. 5a), a well-defined track does not form in the deep boundary layer, with characteristic cloud cell sizes of 30–40 km (Fig. 5b). A ship track is also not detected in $N_{\mathrm{d\_top}}$ or $R_{\mathrm{reff\_top}}$ (Fig.3b and c, respectively). The absence of a track in the deep boundary layer is largely attributed to (i) the large spatial scales of variability within the background cloud state which is determined by the cloud dynamics and cloud-field organisation, and (ii) the incomplete filling in of the detrained cloud amount between cell walls, which prevents the transition to a 100 % cloud-covered state.

A change in A_{cld} of 0.15, which is of the same magnitude as previously identified in ship tracks (Christensen and Stephens, 2011; Goren and Rosenfeld, 2012; Wang et al., 2011), is found embedded in deep open cells of the ship simulation. $N_{\mathrm{d\_top}}$ was increased by 167 % and $R_{\mathrm{eff\_top}}$ decreased by 14 % (Table 2). Yet, these effects remain seemingly hidden in the large variability of the cloud properties governed by the dynamics of the cloud cells. Furthermore, these effects may not easily be attributed to aerosol perturbations via remote sensing techniques of cloud properties as most of the changes in local cloud properties remain within the variability of the system.

Knowing the position and extent of the aerosol perturbation allows one to remove a sufficient amount of variability within the ship simulation to obtain a spatially constrained, detectable and attributable response within the cloud properties. As one averages along the spatial dimension of the aerosol perturbation (coinciding with the x direction of the simulation domain) the pronounced shift in cloud properties between the seeded and unseeded regions of the ship simulation (Fig. 6) is highlighted.

However, while changes in total albedo induced within the seeded region may be identified in this manner, the change in total albedo of 0.03 (Table 2) within the detrained cloud regions of the surrounding unseeded domain would still not be accounted for. Furthermore, changes in A_{cld} within the detrained cloud sheets were found up to 60 km from the emission line, which has implications for the definition of the truly unperturbed albedo within satellite retrievals of such scenes.

4 Implications for aerosol radiative forcing estimates in marine stratocumuli

Estimating the aerosol-induced radiative forcing in low-level marine clouds constitutes a considerable uncertainty in the overall cloud radiative forcing of anthropogenic aerosols. Satellite-based estimates of CRE changes due to ship exhaust have remained inconclusive due to the high degree of variability within the natural cloud scene (Peters et al., 2011). GCM estimates provide a wide range of CRE changes between -0.6 and $-0.07\,\mathrm{W\,m^{-2}}$ (Lauer et al., 2007; Righi et al., 2011; Peters et al., 2012; Partanen et al., 2013) due to open-ocean shipping. Furthermore, it remains unclear whether GCMs represent the relevant scales of variability to provide reliable CRE estimates. The analysis of global datasets of ship tracks (Chen et al., 2015) and volcano plumes (Toll et al., 2017), which have been used as analogues to study the cloud response to anthropogenic emissions, have shown that in the global mean, the cloud response within the tracks largely follows the brightening expected by Twomey (1991). In the global mean, increases and decreases in LWP within the different cloud regimes seem to offset one another, while many GCMs predict a positive LWP response only (Wang et al., 2012; Ghan et al., 2016; Malavelle et al., 2017; Toll et al., 2017).

In this study we demonstrate that non-negligible amounts of brightening due to anthropogenic shipping emissions may persist in the absence of a clear ship track. In deep open cells, perturbations in A_{cld} were found to be as large as 0.15 in regions where $\Delta N_{\mathrm{a\_sub}}$ is high and as large as 0.08 when integrated over the whole simulation domain of $180 \times 180\,\mathrm{km^2}$. Furthermore, the induced brightening, which is almost as high as in simulations displaying a pronounced ship track ($\Delta A_{\mathrm{cld}} = 0.1$ in Wang et al., 2011) remains obscured by the variability of the unpolluted cloud, where LWP and $N_{\mathrm{d\_top}}$ in itself may differ by an order of magnitude between convective cell walls and stratified regions of detrained cloud (Fig. 2).

Furthermore, while these simulations are highly idealised in their set-up, they do not necessarily reflect unrealistic emission conditions. The prescribed ship is assumed to travel periodically along an identical emission line without any crosswind, which may alter the plume size or dilute emissions more effectively. Within the 48 h simulation, a total of five ships traverse the $180 \times 180\,\mathrm{km^2}$ domain repeatedly at a constant sailing speed of $5\,\mathrm{m\,s^{-1}}$, and the cloud response to their combined emissions is assessed. Throughout most of the North Pacific a shipping density of around 30 ships per $100\,\mathrm{km^2}$ per year is observed (MarineTraffic, 2018). Assuming a speed of $5\,\mathrm{m\,s^{-1}}$ (or even $10\,\mathrm{m\,s^{-1}}$), such a density corresponds to an estimated number of 116 (58) ships within the simulation domain on average. Within the North Atlantic, the higher density of ships could even correspond to over 200 (400) ships within a $180 \times 180\,\mathrm{km^2}$ domain (MarineTraffic, 2018). Therefore, our emission scenario is equivalent to merely 1 %–9 % of these ships contributing to increased CCN concentrations within the seeded domain.

Increases in cloud-scene albedo were attributed to changes in brightness within the stratified, detrained cloud regions covering the boundary layer between convective cell walls. These detrained cloud regions are optically thin ($\overline{\tau} = 2.8$) and are often referred to as veil clouds. They are connected to the sub-cloud layer aerosol through the convective cell walls feeding into the detrained cloud regions. In our simulations, these detrained cloud filaments contributed 82 % to the overall cloud fraction.

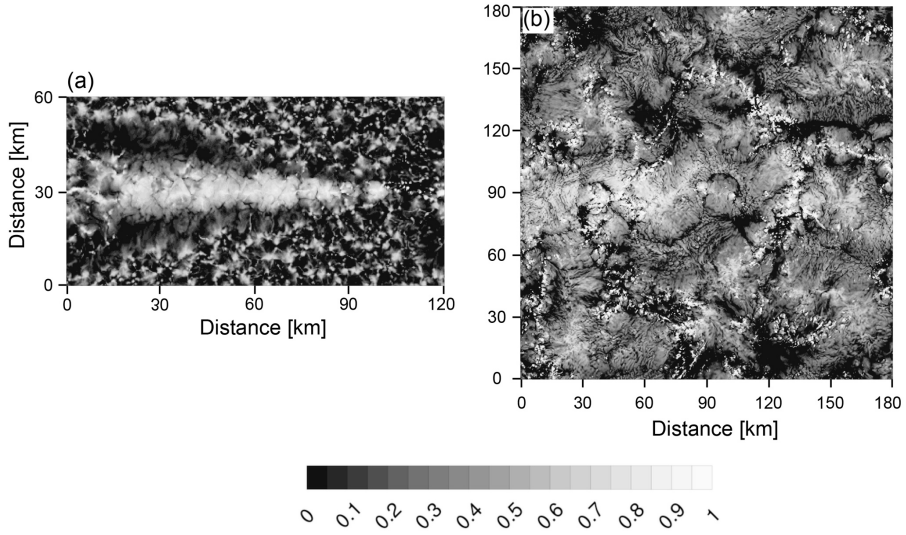

Figure 5. (a) Cloud albedo field from Fig. 1a in Wang et al. (2011) for an 800 m deep boundary layer. **(b)** Cloud albedo at 12:00 UTC on the second day of the ship simulation for a 1.5 km deep boundary layer. Both simulations were subject to an equal seeding source of 10^{17} particles s^{-1}.

In summary, our results suggest that although detectable ship tracks are extremely rare in deep boundary layers, an increase in A_{cld} of the order of 0.1 may persist in deeper boundary layers of open-cell stratocumuli. Furthermore, our simulations suggest that the albedo increase within this regime, which is currently not picked up in ship track analyses, could be driven predominantly by increases in cloud fraction, as opposed to the Twomey (1991) effect.

While these simulations are limited in their generality, they do demonstrate that substantial changes in A_{cld} may occur in optically thin veil clouds and that the aerosol-induced changes in cloud scene albedo may prove extremely difficult to attribute without knowing the spatio-temporal distribution of the aerosol perturbation. Despite significant changes in cloud-scene albedo, an attribution of these changes to an aerosol perturbation using satellite retrievals of cloud-properties and vertically integrated aerosol metrics alone could prove to be extremely difficult in this cloud regime (Fig. 3). Yet such open-cell cloud scenes with a substantial cloud fraction and a high percentage of veil clouds occur often (McCoy et al., 2017) and occur in regions of high solar insolation. Therefore, aerosol-induced cloud radiative perturbations within these clouds may be relevant to global estimates of aerosol–cloud radiative forcing.

Our results strongly motivate further research into the efficacy of aerosol perturbations in deep open-cell stratocumulus. Here we demonstrate that the aerosol forcing in this regime could be substantial. Yet for a clear assessment the occurrence rate and magnitude of A_{cld} changes in stratified detrained cloud remnants need to be known. One approach to constrain these aerosol-induced perturbations could be field measurements around known aerosol perturbations. Such measurements would allow the detection and attribution of cloud radiative effects to aerosol perturbations.

5 Conclusions

The analysis of ship tracks and changes in cloud radiative properties within them has arguably provided an extremely useful framework to develop a mechanistic understanding of aerosol–cloud radiative interactions and to constrain the effective cloud radiative forcing within marine low-level clouds. However, linear shaped tracks are extremely rare and tend to form in shallow boundary layers with a top below 800 m (Durkee et al., 2000b; Christensen and Stephens, 2012; Chen et al., 2015; Toll et al., 2017).

At least 70 % of marine stratocumuli form in deeper boundary layers, where distinct ship tracks due to ship emissions are very rarely detected. Furthermore, 73 % of all stratocumuli globally are likely to occur within the open-cell or disorganised regime (Muhlbauer et al., 2014). Here, we assessed in idealised cloud-resolving simulations whether significant cloud radiative perturbations persist in a field of deep (boundary layer top at 1.5 km) open-cell stratocumulus, which was observed during RF06 of the VOCALS-REx campaign. Our key findings are summarised as follows:

1. Albedo changes equivalent to albedo increases in previously observed ship tracks within shallow open-cell stratocumuli were embedded within a stratocumulus deck of deep open cells, despite the absence of a spatially coherent structure such as a ship track. The domain-mean all-sky albedo increased by 0.05 due to a prescribed seeding source (sea salt emission moving

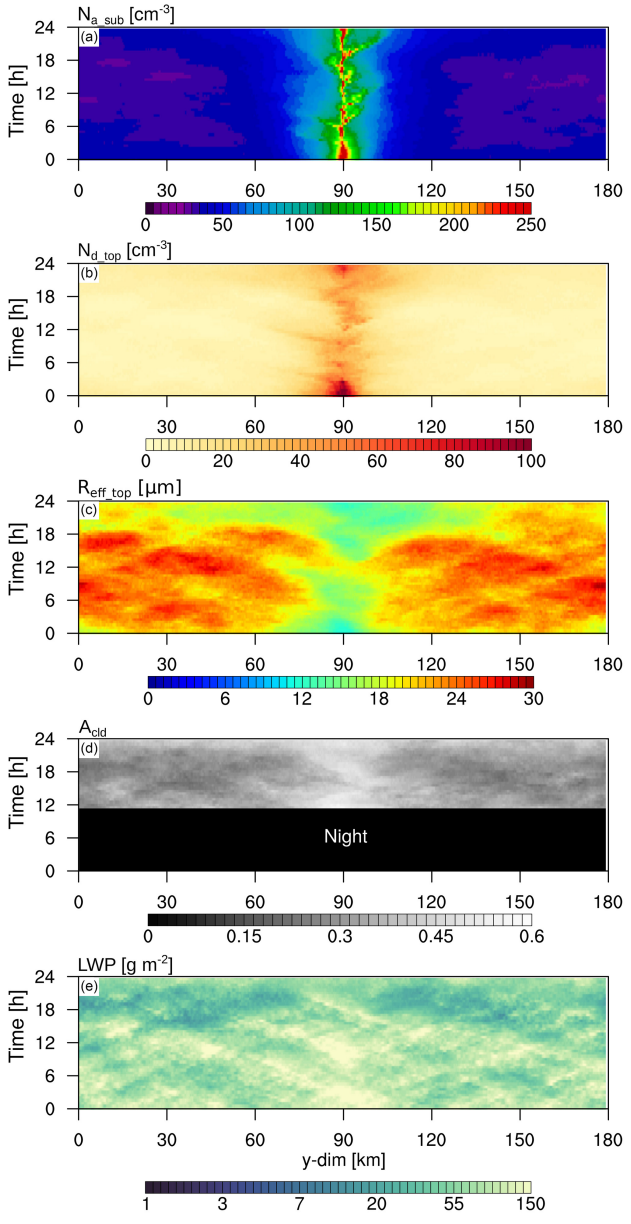

Figure 6. Hovmoeller diagrams of **(a)** sub-cloud layer mean aerosol concentration (N_{a_sub}), **(b)** cloud-top cloud droplet number concentration (N_{d_top}), **(c)** cloud-top mean effective cloud droplet radius (R_{eff_top}), **(d)** cloud albedo (A_{cld}) and **(e)** liquid water path (LWP). Spatial averages were obtained along the emission line dimension (coinciding with x dimension of simulation domain). Hovmoeller diagrams for the ctrl simulation are shown in the Supplement (Fig. S8).

at 5 m s^{-1}, which released particles of 300 nm in size at a rate of 10^{17} particles s^{-1}). This translates to a change in the SW CRE of 20 W m^{-2}, for an annual solar mean insolation of 404 W m^{-2} at this site.

2. Regional changes in A_{cld} (increase by 0.15) and cloud microphysical (167 % increase in N_{d_top} and 14 % decrease in R_{eff_top}) and macrophysical properties (14 % absolute increase in CF and a 5–23 % decrease in in-cloud LWP) within the seeded domain (±30 km around the emission line) remain obscured by the naturally occurring variability of cloud field. Reducing the variability of the clouds by averaging along the spatial extent of the aerosol perturbation permitted the detection and attribution of these cloud radiative effects to the aerosol perturbation. Hence, knowledge of the spatio-temporal distribution of the aerosol perturbation was found to be necessary for the remote attribution of aerosol effects on cloud radiative properties within this regime.

3. The simulated cloud brightening was attributed to the brightening of the detrained cloud filaments that spanned the regions between the convective cell walls of the open cells. These so-called veil clouds occur frequently in low-level cloud layers and are connected to sub-cloud aerosol sources through the convective cloud cores within the cell walls. Within these clouds the brightening was largely attributed to increases in cloud fraction, with a secondary contribution to brightening due to changes in cloud microphysical properties.

Data availability. The simulations for this paper are stored at https://drive.google.com/open?id=1oTrpKtGKfPQBvgYBP3F2xBE4lDkVTpBh, last access: 6 December 2018, and are open acces. The WRF code is open access with public documentation.

Supplement. The supplement related to this article is available online at: https://doi.org/10.5194/acp-18-17475-2018-supplement.

Author contributions. AP, HW, KC, RW and TPA designed the research. AP performed the research. HW contributed code adjustments to WRF. AP analyzed data. AP, HW, KC, RW and TPA wrote the paper.

Competing interests. The authors declare that they have no conflict of interest.

Acknowledgements. We acknowledge the Fund for Innovative Climate and Energy Research grant for the financial support of this research and the high-performance computing support from Yellowstone (ark:/85065/d7wd3xhc). This support was provided by NCAR's Computational and Information Systems Laboratory, sponsored by the National Science Foundation. Hailong Wang acknowledges support from the U.S. Department of Energy (DOE) Office of Science, Biological and Environmental Research. The Pacific Northwest National Laboratory (PNNL) is operated for DOE by Battelle Memorial Institute under contract DE-AC05-76RLO1830.

Edited by: Patrick Chuang
Reviewed by: two anonymous referees

References

Berner, A. H., Bretherton, C. S., and Wood, R.: Large eddy simulation of ship tracks in the collapsed marine boundary layer: a case study from the Monterey Area Ship Track Experiment, Atmos. Chem. Phys., 15, 5851–5871, https://doi.org/10.5194/acp-15-5851-2015, 2015.

Boucher, O., Randall, D., Artaxo, P., Bretherton, C., Feingold, G., Forster, P., Kerminen, V.-M., Kondo, Y., Liao, H., Lohmann, U., Rasch, P., Satheesh, S. K., Sherwood, S., Stevens, B., and Zhang, X. Y.: Clouds and Aerosols, in: Climate Change 2013: The physical science basis. Contribution of Working Group I to the Fifth Assessment Report of the Intergovernmental Panel on Climate Change, edited by: Stocker, T., Qin, D., Plattner, G.-K., Tignor, M., Allen, S., Boschung, J., Nauels, A., Xia, Y., Bex, V., and Midgley, P. M., Cambridge University Press, Cambridge, 2013.

Campmany, E., Grainger, R. G., Dean, S. M., and Sayer, A. M.: Automatic detection of ship tracks in ATSR-2 satellite imagery, Atmos. Chem. Phys., 9, 1899–1905, https://doi.org/10.5194/acp-9-1899-2009, 2009.

Charlson, R. J., Ackerman, A. S., Bender, F. A.-M., Anderson, T. L., and Liu, Z.: On the climate forcing consequences of the albedo continuum between cloudy and clear air, Tellus B, 59, 715–727, https://doi.org/10.1111/j.1600-0889.2007.00297.x, 2007.

Chen, G., Wang, W.-C., and Chen, J.-P.: Aerosol-stratocumulus-radiation interactions over the southeast Pacific, J. Atmos. Sci., 72, 2612–2621, 2015.

Chen, Y.-C., Christensen, M. W., Xue, L., Sorooshian, A., Stephens, G. L., Rasmussen, R. M., and Seinfeld, J. H.: Occurrence of lower cloud albedo in ship tracks, Atmos. Chem. Phys., 12, 8223–8235, https://doi.org/10.5194/acp-12-8223-2012, 2012.

Christensen, M. and Stephens, G.: Microphysical and macrophysical responses of marine stratocumulus polluted by underlying ships: 2. Impacts of haze on precipitating clouds, J. Geophys. Res., 116, D11203, https://doi.org/10.1029/2010JD014638, 2011.

Christensen, M. and Stephens, G.: Microphysical and macrophysical responses of marine stratocumulus polluted by underlying ships: evidence of cloud deepening, J. Geophys. Res., 117, D03201, https://doi.org/10.1029/2011JD017125, 2012.

Coakley, J. A. and Walsh, C. D.: Limits to the aerosol indirect radiative effect derived from observations of ship tracks, J. Atmos. Sci., 59, 668–680, 2002.

Conover, J. H.: Anomalous cloud lines, J. Atmos. Sci., 23, 778–785, 1966.

Durkee, P. A., Chartier, R. E., Brown, A., Trehubenko, E. J., Rogerson, S. D., Skupniewicz, C., and Nielsen, K. E.: Composite Ship Track Characteristics, J. Atmos. Sci., 57, 2542–2553, 2000a.

Durkee, P. A., Noone, K. J., and Bluth, R. T.: The Monterey Area Ship Track Experiment, J. Atmos. Sci., 57, 2523–2541, 2000b.

Durkee, P. A., Noone, K. J., Ferek, R. J., Johnson, D. W., Taylor, J. P., Garrett, T. J., Hobbs, P. V., Hudson, J. G., Bretherton, C. S., Innis, G., Frick, G. M., Hoppel, W. A., O'Dowd, C. D., Russel, L. M., Gasparovic, R., Nielsen, K. E., Tessmer, S. A., Öström, E., Osborne, S. R., Flagan, R. C., Seinfeld, J. H., and Rand, H.: The impact of ship-produced aerosols on the microstructure and albedo of warm marine stratocumulus clouds: A test of MAST hypothesis 1i and 1ii, J. Atmos. Sci., 57, 2542–2553, 2000c.

European Maritime Safety Agency: Equasis Statistics – The world merchant fleet in 2014, available at: http://www.emsa.europa.eu/ (last access: 21 February 2018), 2014.

Feingold, G., Koren, I., Yamaguchi, T., and Kazil, J.: On the reversibility of transitions between closed and open cellular convection, Atmos. Chem. Phys., 15, 7351–7367, https://doi.org/10.5194/acp-15-7351-2015, 2015.

Ghan, S., Wang, M., Zhang, S., Ferrachat, S., Gettelman, A., Griesfeller, J., Kipling, Z., Lohmann, U., Morrison, H., Neubauer, D., Partridge, D. G., Stier, P., Takemura, T., Wang, H., and Zhang, K.: Challenges in constraining anthropogenic aerosol effects on cloud radiative forcing using present-day spatiotemporal variability, P. Natl. Acad. Sci. USA, 113, 5804–5811, https://doi.org/10.1073/pnas.1514036113, 2016.

Goren, T. and Rosenfeld, D.: Satellite observations of ship emissions induced transitions from broken to closed cell marine stratocumulus over large areas, J. Geophys. Res., 117, D17206, https://doi.org/10.1029/2012JD017981, 2012.

Kazil, J., Wang, H., Feingold, G., Clarke, A. D., Snider, J. R., and Bandy, A. R.: Modeling chemical and aerosol processes in the transition from closed to open cells during VOCALS-REx, Atmos. Chem. Phys., 11, 7491–7514, https://doi.org/10.5194/acp-11-7491-2011, 2011.

Khairoutdinov, M. and Kogan, Y.: A new cloud physics parameterization in a large-eddy simulation model of marine stratocumulus, Mon. Weather Rev., 128, 229–243, https://doi.org/10.1175/1520-0493(2000)128<0229:ANCPPI>2.0.CO;2, 2000.

Koren, I., Remer, L. A., Kaufman, Y. J., Rudich, Y., and Martins, J. V.: On the twilight zone between clouds and aerosols, Geophys. Res. Lett., 34, l08805, https://doi.org/10.1029/2007GL029253, 2007.

Kravitz, B., Wang, H., Rasch, P., Morrison, H., and Solomon, A.: Process-model simulations of cloud albedo enhancement by aerosols in the Arctic, Phil. T. R. Soc. A, 372, 1–24, https://doi.org/10.1098/rsta.2014.0052, 2014.

Lauer, A., Eyring, V., Hendricks, J., Jöckel, P., and Lohmann, U.: Global model simulations of the impact of ocean-going ships on aerosols, clouds, and the radiation budget, Atmos. Chem. Phys., 7, 5061–5079, https://doi.org/10.5194/acp-7-5061-2007, 2007.

Malavelle, F. F., Haywood, J. M., Jones, A., Gettelman, A., Clarisse, L., Bauduin, S., Allan, R. P., Karset, I. H. H., Kristjánsson, J. E., Oreopoulos, L., Cho, N., Lee, D., Bellouin, N., Boucher, O., Grosvenor, D. P., Carslaw, K. S., Dhomse, S., Mann, G. W., Schmidt, A., Coe, H., Hartley, M. E., Dalvi, M., Hill, A. A., Johnson, B. T., Johnson, C. E., Knight, J. R., O'Connor, F. M., Partridge, D. G., Stier, P., Myhre, G., Platnick, S., Stephens, G. L., Takahashi, H., and Thordarson, T.: Erratum: Strong constraints on aerosol–cloud interactions from volcanic eruptions, Nature, 546, 485–491, https://doi.org/10.1038/nature24275, 2017.

MarineTraffic: Marine Traffic Database, available at: https://www.marinetraffic.com, last access: 19 September 2018.

McCoy, I. L., Wood, R., and Fletcher, J. K.: Identifying meteorological controls on open and closed mesoscale cellular convection associated with marine cold air out-

breaks, J. Geophys. Res.-Atmos., 122, 11678–11702, https://doi.org/10.1002/2017JD027031, 2017.

Morrison, H., Thompson, G., and Tatarskii, V.: Impact of cloud microphysics on the development of trailing stratiform precipitation in a simulated squall line: comparison of one- and two-moment schemes, Mon. Weather Rev., 137, 991–1007, https://doi.org/10.1175/2008MWR2556.1, 2009.

Muhlbauer, A., McCoy, I. L., and Wood, R.: Climatology of stratocumulus cloud morphologies: microphysical properties and radiative effects, Atmos. Chem. Phys., 14, 6695–6716, https://doi.org/10.5194/acp-14-6695-2014, 2014.

Myhre, G., Shindell, D., Bréon, F.-M., Collins, W., Fuglestvedt, J., Huang, J., Koch, D., Lamarque, J.-F., Lee, D., Mendoza, B., Nakajima, T., Robock, A., Stephens, G., Takemura, T., and Zhang, H.: Anthropogenic and natural radiative forcing, book section 8, 659–740, Cambridge University Press, Cambridge, United Kingdom and New York, NY, USA, https://doi.org/10.1017/CBO9781107415324.018, 2013.

Nam, C., Bony, S., Dufresne, J.-L., and Chepfer, H.: The 'too few, too bright' tropical low-cloud problem in CMIP5 models, Geophys. Res. Lett., 39, L21801, https://doi.org/10.1029/2012GL053421, 2012.

NASA: SeaWinds on QuickSCAT Level 3 surface wind speed for climate model comparison, Ver. 1. PO.DAAC, CA, USA, https://doi.org/10.5067/QSSWS-CMIP1, 2012.

Partanen, A. I., Laakso, A., Schmidt, A., Kokkola, H., Kuokkanen, T., Pietikäinen, J.-P., Kerminen, V.-M., Lehtinen, K. E. J., Laakso, L., and Korhonen, H.: Climate and air quality trade-offs in altering ship fuel sulfur content, Atmos. Chem. Phys., 13, 12059–12071, https://doi.org/10.5194/acp-13-12059-2013, 2013.

Peters, K., Quaas, J., and Graßl, H.: A search for large-scale effects of ship emissions on clouds and radiation in satellite data, J. Geophys. Res., 116, D24205, https://doi.org/10.1029/2011JD016531, 2011.

Peters, K., Stier, P., Quaas, J., and Graßl, H.: Aerosol indirect effects from shipping emissions: sensitivity studies with the global aerosol-climate model ECHAM-HAM, Atmos. Chem. Phys., 12, 5985–6007, https://doi.org/10.5194/acp-12-5985-2012, 2012.

Platnick, S. and Twomey, S.: Determining the susceptibility of cloud albedo to changes in droplet concentration with the Advanced Very High Resolution Radiometer, J. Appl. Meteorol., 33, 334–347, https://doi.org/10.1175/1520-0450(1994)033<0334:DTSOCA>2.0.CO;2, 1994.

Righi, M., Klinger, C., Eyring, V., Hendricks, J., Lauer, A., and Petzold, A.: Climate impact of biofuels in shipping: global model studies of the aerosol indirect effect, Environ. Sci. Technol., 45, 3519–3525, 2011.

Salter, S., Sortino, G., and Latham, J.: Sea-going hardware for the cloud albedo method of reversing global warming, Philos. T. R. Soc. A, 366, 3989–4006, https://doi.org/10.1098/rsta.2008.0136, 2008.

Schneider, T., Teixeira, J., Bretherton, C. S., Pressel, K. G., Schär, C., and Siebesma, A. P.: Climate goals and computing the future of clouds, Nat. Clim. Change, 7, 3–5, https://doi.org/10.1038/nclimate3190, 2017.

Schreier, M., Kokhanovsky, A. A., Eyring, V., Bugliaro, L., Mannstein, H., Mayer, B., Bovensmann, H., and Burrows, J. P.: Impact of ship emissions on the microphysical, optical and radiative properties of marine stratus: a case study, Atmos. Chem. Phys., 6, 4925–4942, https://doi.org/10.5194/acp-6-4925-2006, 2006.

Schreier, M., Mannstein, H., Eyring, V., and Bovensmann, H.: Global ship track distribution and radiative forcing from 1 year of AATSR data, Geophys. Res. Lett., 34, L17814, https://doi.org/10.1029/2007GL030664, 2007.

Terai, C. R., Bretherton, C. S., Wood, R., and Painter, G.: Aircraft observations of aerosol, cloud, precipitation, and boundary layer properties in pockets of open cells over the Southeast Pacific, Atmos. Chem. Phys., 14, 8071–8088, https://doi.org/10.5194/acp-14-8071-2014, 2014.

Toll, V., Christensen, M., Gassó, S., and Bellouin, N.: Volcano and ship tracks indicate excessive aerosol-induced cloud water increases in a climate model, Geophys. Res. Lett., 44, 12492–12500, https://doi.org/10.1002/2017GL075280, 2017.

Twomey, S.: Aerosols, clouds and radiation, Atmos. Environ., 25, 2435–2442, 1991.

Wang, H. and Feingold, G.: Modeling mesoscale cellular structures and drizzle in marine stratocumulus. Part II: Microphysics and dynamcis of the boundary region between open and closed cells, J. Atmos. Sci., 66, 3257–3275, 2009.

Wang, H., Feingold, G., Wood, R., and Kazil, J.: Modelling microphysical and meteorological controls on precipitation and cloud cellular structures in Southeast Pacific stratocumulus, Atmos. Chem. Phys., 10, 6347–6362, https://doi.org/10.5194/acp-10-6347-2010, 2010.

Wang, H., Rasch, P. J., and Feingold, G.: Manipulating marine stratocumulus cloud amount and albedo: a process-modelling study of aerosol-cloud-precipitation interactions in response to injection of cloud condensation nuclei, Atmos. Chem. Phys., 11, 4237–4249, https://doi.org/10.5194/acp-11-4237-2011, 2011.

Wang, M., Ghan, S., Liu, X., L'Ecuyer, T. S., Zhang, K., Morrison, H., Ovchinnikov, M., Easter, R., Marchand, R., Chand, D., Quian, Y., and Penner, J. E.: Constraining cloud lifetime effects of aerosols using A-Train satellite observations, Geophys. Res. Lett., 39, 15, https://doi.org/10.1029/2012GL052204, 2012.

Wood, R.: Drizzle in Stratiform Boundary Layer Clouds. Part II: Microphysical Aspects, J. Atmos. Sci., 62, 3034–3050, https://doi.org/10.1175/JAS3530.1, 2005.

Wood, R.: Review: Stratocumulus Clouds, Mon. Weather Rev., 140, 2373–2423, 2012.

Wood, R. and Hartmann, D. L.: Spatial Variability of Liquid Water Path in Marine Low Cloud: The Importance of Mesoscale Cellular Convection, J. Climate, 19, 1748–1764, https://doi.org/10.1175/JCLI3702.1, 2006.

Wood, R., Bretherton, C. S., Leon, D., Clarke, A. D., Zuidema, P., Allen, G., and Coe, H.: An aircraft case study of the spatial transition from closed to open mesoscale cellular convection over the Southeast Pacific, Atmos. Chem. Phys., 11, 2341–2370, https://doi.org/10.5194/acp-11-2341-2011, 2011a.

Wood, R., Mechoso, C. R., Bretherton, C. S., Weller, R. A., Huebert, B., Straneo, F., Albrecht, B. A., Coe, H., Allen, G., Vaughan, G., Daum, P., Fairall, C., Chand, D., Gallardo Klenner, L., Garreaud, R., Grados, C., Covert, D. S., Bates, T. S., Krejci, R., Russell, L. M., de Szoeke, S., Brewer, A., Yuter, S. E., Springston, S. R., Chaigneau, A., Toniazzo, T., Minnis, P., Palikonda, R., Abel, S. J., Brown, W. O. J., Williams, S., Fochesatto, J., Brioude, J., and Bower, K. N.: The VAMOS Ocean-Cloud-Atmosphere-

Land Study Regional Experiment (VOCALS-REx): goals, platforms, and field operations, Atmos. Chem. Phys., 11, 627–654, https://doi.org/10.5194/acp-11-627-2011, 2011b.

Wood, R., O, K.-T., Christopher, S. B., Mohrmann, J., Albrecht, B. A., Zuidema, P., Ghate, V., Schwartz, C., Eloranta, E., Glienke, S., Shaw, R., Fugal, J., and Minnis, P.: Ultra-clean layers and optically thin clouds in the stratocumulus to cumulus transition: part I. Observations, J. Atmos. Sci., 0, https://doi.org/10.1175/JAS-D-17-0213.1, 2018.

Zuidema, P., Redemann, J., Haywood, J., Wood, R., Piketh, S., Hipondoka, M., and Formenti, P.: Smoke and clouds above the Southeast Atlantic: Upcoming field campaigns probe absorbing aerosol's impact on climate, B. Am. Meteorol. Soc., 97, 1131–1135, https://doi.org/10.1175/BAMS-D-15-00082.1, 2016.